

Electronic properties of sculptureenes

This content has been downloaded from IOPscience. Please scroll down to see the full text.

2014 New J. Phys. 16 013060

(<http://iopscience.iop.org/1367-2630/16/1/013060>)

View [the table of contents for this issue](#), or go to the [journal homepage](#) for more

Download details:

IP Address: 148.88.211.31

This content was downloaded on 15/12/2014 at 10:11

Please note that [terms and conditions apply](#).

Electronic properties of sculpturenes

Laith Algharagholy¹, Thomas Pope², Steven W D Bailey²
and Colin J Lambert^{2,3}

¹ Computer Science and Mathematics College, University of Al-Qadisiyah, Diwaniyah, Iraq

² Department of Physics, Lancaster University, Lancaster LA1 4YB, UK

E-mail: c.lambert@lancaster.ac.uk

Received 14 September 2013, revised 17 December 2013

Accepted for publication 19 December 2013

Published 31 January 2014

New Journal of Physics **16** (2014) 013060

doi:[10.1088/1367-2630/16/1/013060](https://doi.org/10.1088/1367-2630/16/1/013060)

Abstract

We investigate the electronic properties of *sculpturenes*, formed by sculpting selected shapes from bilayer graphene, boron nitride or graphene–boron nitride hetero-bilayers and allowing the shapes to spontaneously reconstruct. The simplest sculpturenes are periodic nanotubes, containing lines of non-hexagonal rings. More complex sculpturenes formed from shapes with non-trivial topologies, connectivities and materials combinations may also be constructed. Results are presented for the reconstructed geometries, electronic densities of states and current–voltage relations of these new structures.

 Online supplementary data available from stacks.iop.org/NJP/16/013060/mmedia

1. Introduction

Sculpturenes are novel nanometre-scale objects, obtained by cutting selected shapes from layered materials and allowing the shapes to reconstruct [1, 2]. The simplest examples of sculpturenes are formed by cutting straight nanoribbons (NRs) from bilayer graphene (BiGR) and allowing the edges to reconstruct to maximize sp^2 bonding. If the width of the NR is sufficiently small (i.e. of order 3 nm or less) then the whole ribbon can reconstruct to form a carbon nanotube (CNT), with a pre-defined location and chirality. More complex all-carbon structures with unique topologies are also possible, as are *T*-shapes, crosses and other multiply-connected structures. By sculpting hetero-bilayers such as graphene on monolayer boron nitride

³ Author to whom any correspondence should be addressed.



Content from this work may be used under the terms of the [Creative Commons Attribution 3.0 licence](http://creativecommons.org/licenses/by/3.0/). Any further distribution of this work must maintain attribution to the author(s) and the title of the work, journal citation and DOI.

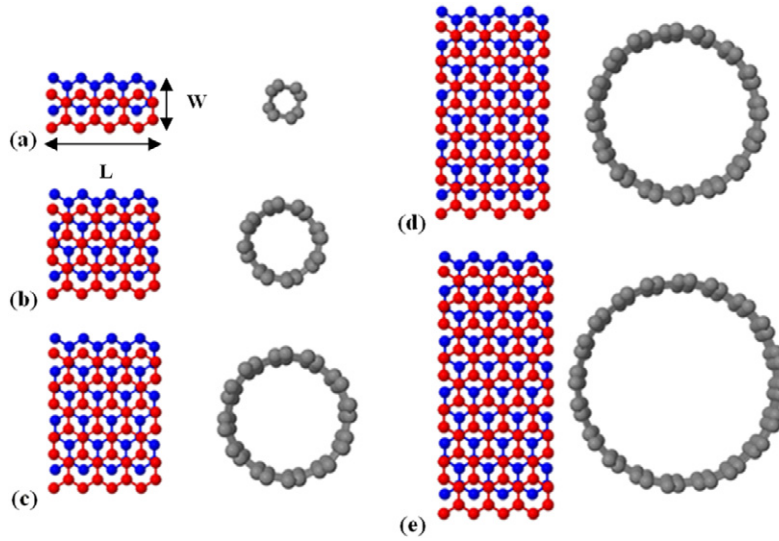


Figure 1. Armchair CNTs obtained by relaxing AB-stacked BiZGNRs with different widths W . The ribbons are infinitely periodic in the horizontal direction and to allow the possibility of surface reconstruction, supercells of length $L = 3.5 \times 3^{1/2} a_{c-c}$ are employed, where $a_{c-c} = 1.44 \text{ \AA}$ is the carbon-carbon bond length. (a) $W = 3 a_{c-c}$ relaxes to a (2,2) armchair CNT. (b) $W = 6 a_{c-c}$ relaxes to a (4,4) armchair CNT. (c) $W = 9 a_{c-c}$ relaxes to a (6,6) armchair CNT. (d) $W = 12 a_{c-c}$ relaxes to a (8,8) armchair CNT. (e) $W = 15 a_{c-c}$ relaxes to a (10,10) armchair CNT. See movie 1, available at stacks.iop.org/NJP/16/013060/mmedia.

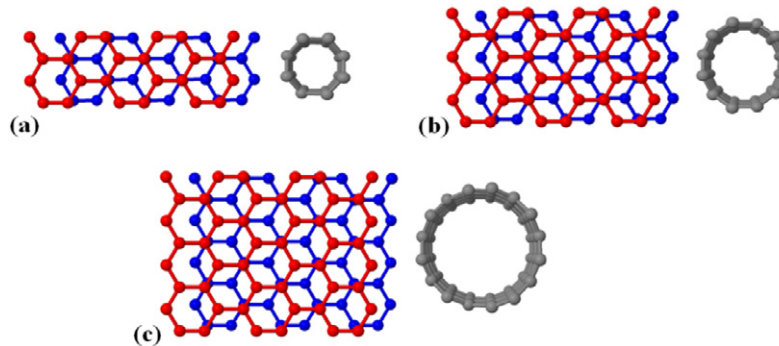


Figure 2. Zigzag CNTs obtained by relaxing AB-stacked BiAGNRs with different widths W . The ribbons are infinitely periodic in the horizontal direction and to allow the possibility of surface reconstruction, supercells of length $L = 8 a_{c-c}$ are employed. (a) $W = 1.5 \times 3^{1/2} a_{c-c}$ relaxes to a (4,0) zigzag CNT. (b) $W = 2.5 \times 3^{1/2} a_{c-c}$ relaxes to a (6,0) zigzag CNT. (c) $W = 3.5 \times 3^{1/2} a_{c-c}$ relaxes to an (8,0) zigzag CNT.

(BN) and allowing them to reconstruct, new hetero-nanotubes (NTs) can be made, as well as a variety of more complex geometries formed from two or more materials.

In practice, a variety of techniques are available for cutting sculpturenes [3]. For example graphene can be cut using lithographic [4–6], chemical [7–10] and sonochemical [11, 12] techniques. In particular, scanning tunnelling microscopy lithography [6] can be used to cut graphene nanoribbons (GNRs) with widths as small as 2.5 nm, with a specified chirality, a specified location and with their ends contacted to (graphene) electrodes and aberration-corrected transmission electron microscopy can be used to cut holes in graphene and other

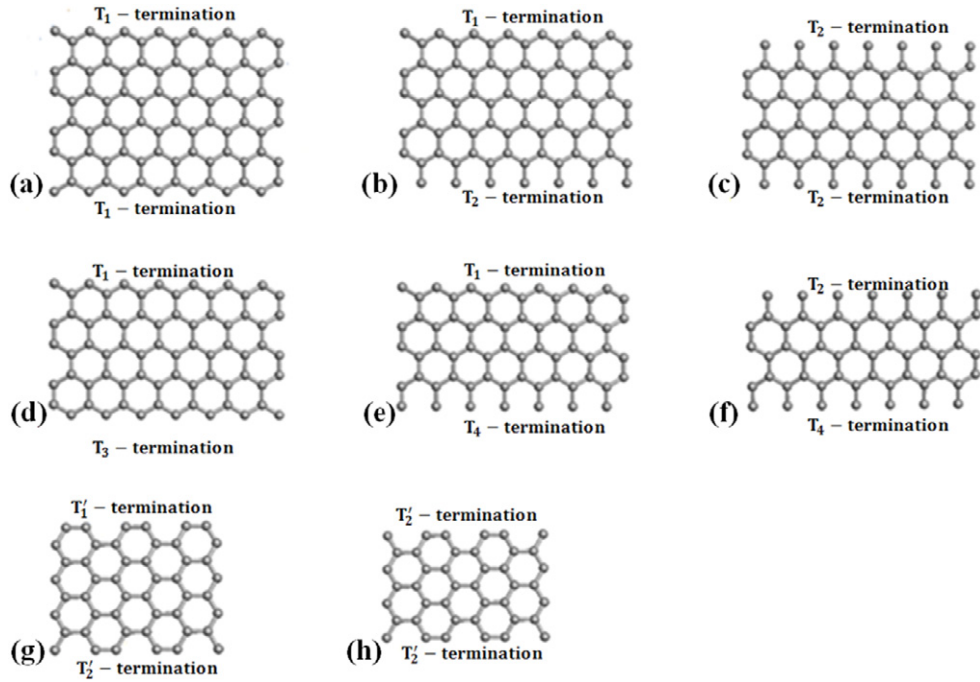


Figure 3. Panels (a)–(f) Supercells of monolayer ZGNRs (periodic in horizontal direction) with various widths W and identical lengths. Six ZGNR terminations are shown, (a) T_1T_1 -termination (84 atoms) with $W = 8a_{c-c}$. (b) T_1T_2 -termination (77 atoms) with $W = 7.5a_{c-c}$. (c) T_2T_2 -termination (70 atoms) with $W = 7a_{c-c}$. (d) T_1T_3 -termination (70 atoms) with $W = 6.5a_{c-c}$. (e) T_1T_4 -termination (63 atoms) with $W = 6a_{c-c}$. (f) T_2T_4 -termination (56 atoms) with $W = 7a_{c-c}$. Panels (g)–(h) show supercells of AGNRs with width W and identical lengths. Two terminations are shown. (g) $T_1' T_2'$ -termination (48 atoms) with $W = 3.5 \times 3^{1/2}a_{c-c}$. (h) $T_2' T_2'$ -termination (42 atoms) with $W = 3 \times 3^{1/2}a_{c-c}$.

materials [13, 14]. All of these require specific experimental conditions and deliver cuts with different levels of accuracy. The atomic-scale dynamics of these methodologies are largely unknown and therefore in what follows, we circumvent this issue by starting from bi-layers with pre-cut edges and then using density functional theory (DFT) to allow them to reconstruct.

The aim of the present paper is to investigate the electron transport properties of a selection of these novel structures. Initially we shall examine the electronic properties of sculpturenes formed by cutting straight bilayer NRs and allowing them to relax. Depending on the direction of cutting, the resulting sculpturenes can be either perfect NTs, or NTs with lines of non-hexagonal rings. Electronic properties of more complex sculpturenes are also presented, including their densities of states and electron transport properties.

2. Electronic and geometric properties of all-carbon sculpturenes formed from straight nanoribbons (NRs)

In what follows, all structures are relaxed using the SIESTA implementation of DFT [15] using the Ceperley–Alder exchange correlation functional, with norm-conserving pseudopotentials and double zeta polarized basis sets of pseudo atomic orbitals.

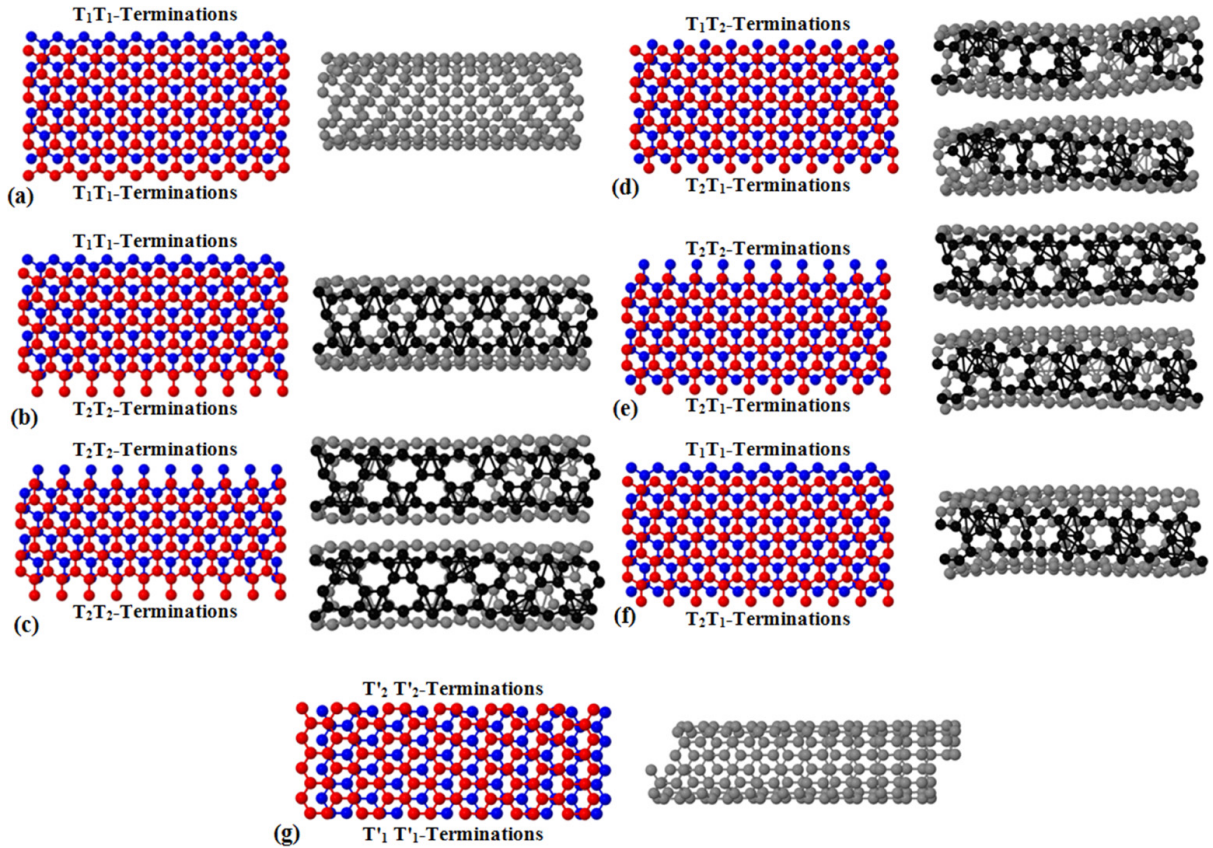


Figure 4. Panels (a)–(g) show AB-stacked BiZGNRs with different edge terminations of the top ZGNR (red) and bottom ZGNR (blue). (a) Shows a supercell with T_1T_1/T_1T_1 -terminations, comprising 240 carbon atoms. (b) T_1T_1/T_2T_2 -terminations (220 carbon atoms). (c) T_2T_2/T_2T_2 -terminations (200 carbon atoms). (d) T_1T_2/T_1T_2 -terminations (220 carbon atoms). (e) T_2T_2/T_1T_2 -terminations (210 carbon atoms). (f) T_1T_1/T_1T_2 -terminations (230 carbon atoms). (g) A BiAGNR with $T'_1T'_1/T'_2T'_2$ -terminations (96 atoms) where the top AGNR is blue and the bottom AGNR is red. After reconstruction, the edges reconstruction is shown in black. In general, we adopt the notation that a BiGNR with T_iT_j/T_kT_l -terminations has a bottom (top) GNR with upper and lower edge terminations T_i and T_k (T_j and T_l).

Figure 1 shows examples of pre-cut, straight, bilayer graphene nanoribbons (BiGNRs), which are infinitely periodic in the horizontal direction and of finite width W in the vertical direction, along with the corresponding NTs, which form after allowing them to reconstruct spontaneously. The initial BiGNRs are AB-stacked bilayer zigzag graphene nanoribbons (BiZGNRs), which after relaxation form perfect armchair CNTs with no defects.

As further examples, figure 2 shows three sculpted AB-stacked bilayer armchair graphene nanoribbons (BiAGNRs), which after reconstruction form perfect zigzag CNTs.

The above examples are only a subset of the CNTs that can be obtained by relaxing armchair or zigzag BiGNRs, because the resulting CNTs depend not only on the orientation of the BiGNR, but also on the combination of edges which coalesce during reconstruction. To illustrate how different combinations of edge terminations can affect the resulting CNTs, consider first the zigzag and armchair edge terminations of GNRs, shown in figure 3.

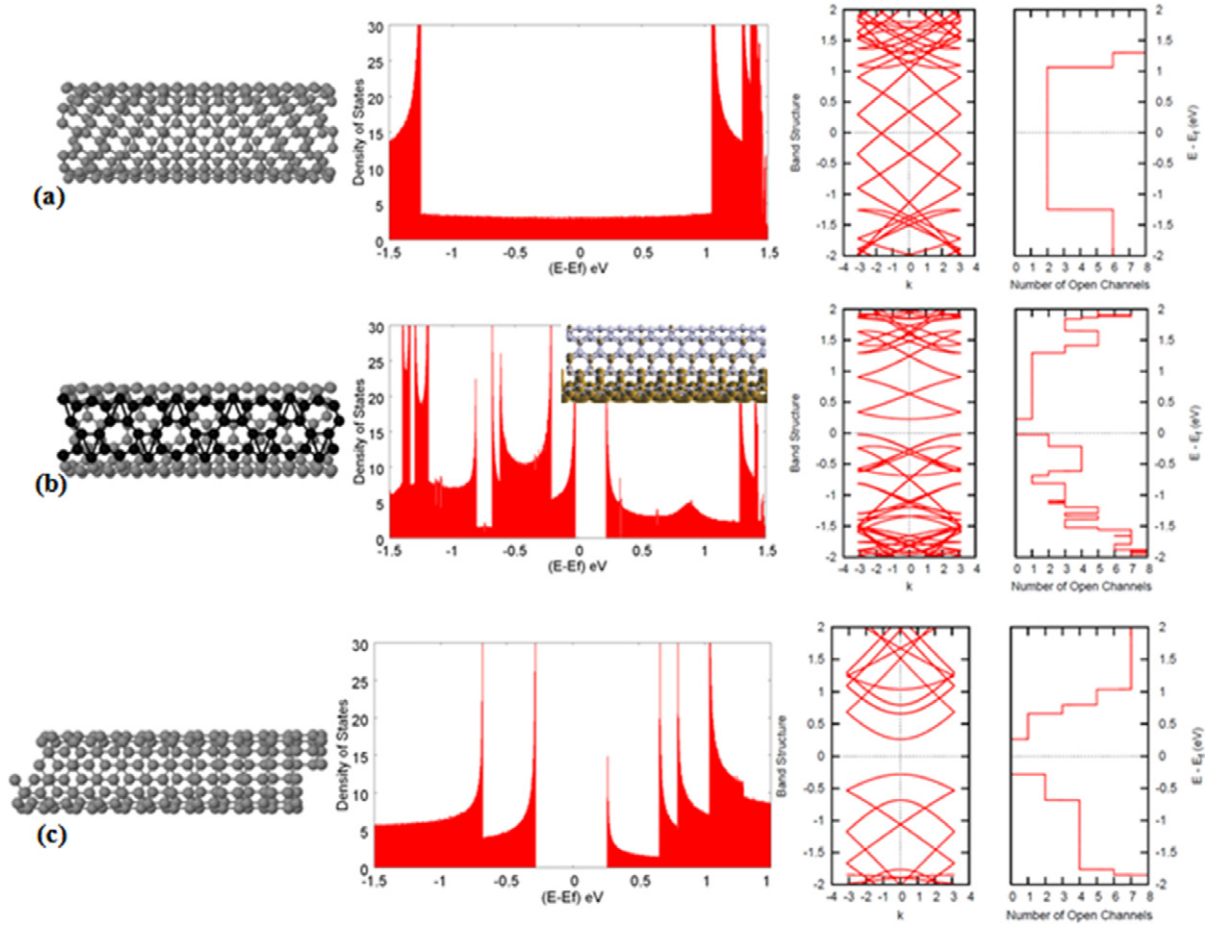


Figure 5. It shows the DOS, band structure and number of open channels for ordered CNT sculpturenes. (a) A perfect (6,6) CNT sculpturene. (b) A CNT sculpturene with one line of 5/7 pairs. (c) A perfect (8,0) CNT sculpturene. The DOS was calculated using 3000 k-points. The middle pane of figure 5(b) also shows the LDOS around the Fermi energy, which is concentrated along the line of defects. For illustrative purposes, the structure is rotated by 90° towards the bottom of the page. The LDOS distribution around the Fermi energy is seen to lie along the line of 5/7 pairs.

Figures 3(a)–(f) show six possible upper and lower edge combinations of monolayer zigzag-terminated GNRs (ZGNRs), formed from edge terminations labelled T_1 , T_2 , T_3 and T_4 . Figures 3(g)–(h) show two possible edge combinations of armchair-terminated GNRs (AGNRs) labelled T'_1 and T'_2 .

When an AB-stacked bilayer is cut to form BiZGNRs, the bilayer NRs possess two upper and two lower edges associated with each of the stacked monolayer ribbons. Each pair of upper (or lower) edges can be formed from a combination of the edges shown in figure 3. For BiZGNRs, examples of these combinations are shown in figures 4(a)–(f), along with the resulting CNTs following reconstruction. Each BiZGNR possesses a pair of upper-edge and lower-edge terminations. For example in figure 4(b), these are T_1T_1 and T_2T_2 respectively.

The CNTs shown in figures 4(a)–(g) are the relaxed structures resulting from each of their adjacent BiGNRs. To perform the geometry relaxation, it is necessary to define a supercell in the initial BiGNR. Since the reconstructed sculpturene may have a larger unit cell than the initial

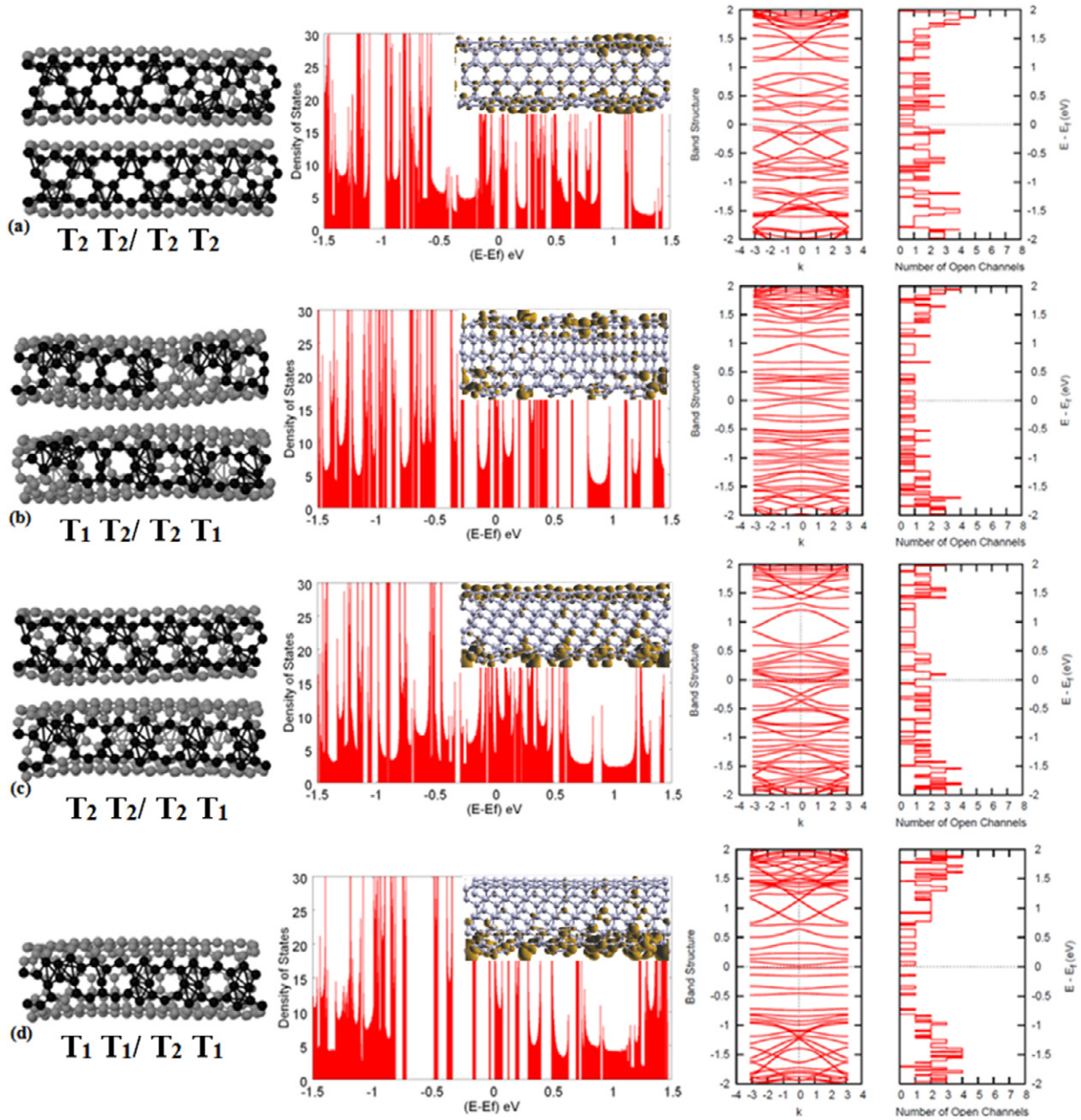


Figure 6. Panels (a)–(c) show the DOS, band structure and number of open channels for disordered CNT sculpturenes with two sides of non-hexagonal ring lines. (a) One side with nine vertical pentagon/heptagon pairs per zip-line and second side with eight vertical pentagon/heptagon pairs per zip-line. (b) Two sides with octagons, horizontal pentagon-pairs and vertical pentagon/heptagon pairs per zip-line. (c) One side with nine vertical pentagon/heptagon pairs per zip-line and second side which contains four octagons, one horizontal pentagon-pair and three vertical pentagon-pairs. (d) One line of four octagons, one horizontal pentagon-pair and three vertical pentagon-pairs. The DOS was calculated using 3000 k-points. The middle panes of each figure show the local densities of states of each sculpturene (rotated by 90 degrees to aid visualization) in the vicinity of the Fermi energy.

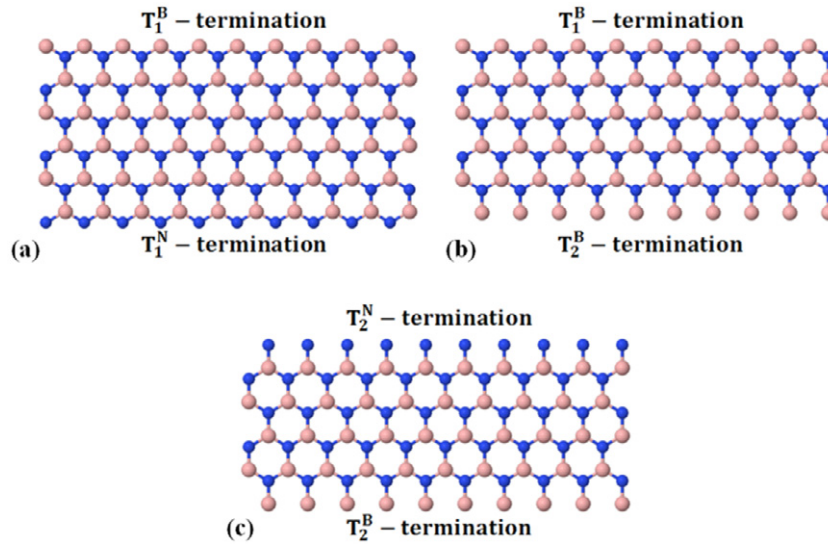


Figure 7. Panels (a)–(c) supercells of monolayer zigzag boron nitride nanoribbon (ZBNNR) bilayer ZBNNR (BiZBNNR) with various widths W and identical lengths. Three ZBNNR terminations are shown. (a) The top edge is terminated with boron T_1^B and the bottom edge is terminated with nitrogen T_1^N (120 nitrogen and boron atoms). (b) The top edge is terminated with boron T_1^B and the bottom edge is terminated with boron T_2^B (110 nitrogen and boron atoms). (c) The top edge is terminated with nitrogen T_2^N and the bottom edge is terminated with nitrogen T_2^B (100 nitrogen and boron atoms). For clarity, nitrogen atom is shown in blue and boron is shown pink.

BiGNR, the supercell is chosen to be larger than the unit cell of the BiGNR and sufficiently large to accommodate the periodicity of the reconstructed sculpture. Although this is not necessary for the sculptures of figures 1 and 2, it is clearly necessary for those of figure 4. Figure 4(g) shows that the $T_1' T_1'/T_2' T_2'$ -terminations relax to a perfect (8,0) zigzag CNT. Further terminations such as $T_1' T_2'/T_1' T_2'$, $T_1' T_1'/T_1' T_2'$ and $T_2' T_2'/T_1' T_2'$ also form a perfect zigzag CNT. This demonstrates that the formation of zigzag CNTs from AGNRs is rather robust. Figure 4(a) shows that $T_1 T_1/T_1 T_1$ terminations of BiZGNRs relax to a perfect (6,6) armchair CNT. Figure 4(b) shows that $T_1 T_1/T_2 T_2$ terminations produce an armchair CNT with a line of pentagon-heptagon pairs. Figure 4(c) shows that $T_2 T_2/T_2 T_2$ terminations produce an armchair CNT with two lines of pentagons-heptagon pairs. Figure 4(d) shows that $T_1 T_2/T_1 T_2$ terminations lead to an armchair CNT with two lines of non-hexagonal rings, which contain octagons, horizontal pentagon-pairs and vertical pentagon-pairs. Figure 4(e) shows that $T_2 T_2/T_1 T_2 T_2'$ terminations lead to two lines of non-hexagonal rings. In this case, the bottom line contains four octagons, one horizontal pentagon-pair and three vertical pentagon-pairs per supercell and the top line contains nine pentagons and heptagons. This tendency for polygons with more than six sides, to be attracted by polygons with less than six sides is a generic topologically-driven feature of networks of three-fold vertices [16, 17]. Figure 4(f) shows that $T_1 T_1/T_1 T_2$ terminations lead to an armchair CNT with one line of four octagons, one horizontal pentagon-pair and three vertical pentagon-pairs per supercell. Such lines of non-hexagonal rings are likely to possess novel spintronic and electronic properties [18–20].

We now investigate the electronic properties of the nanotube (NT) sculptures shown above, all of which are periodic in the horizontal direction, albeit in some cases with large

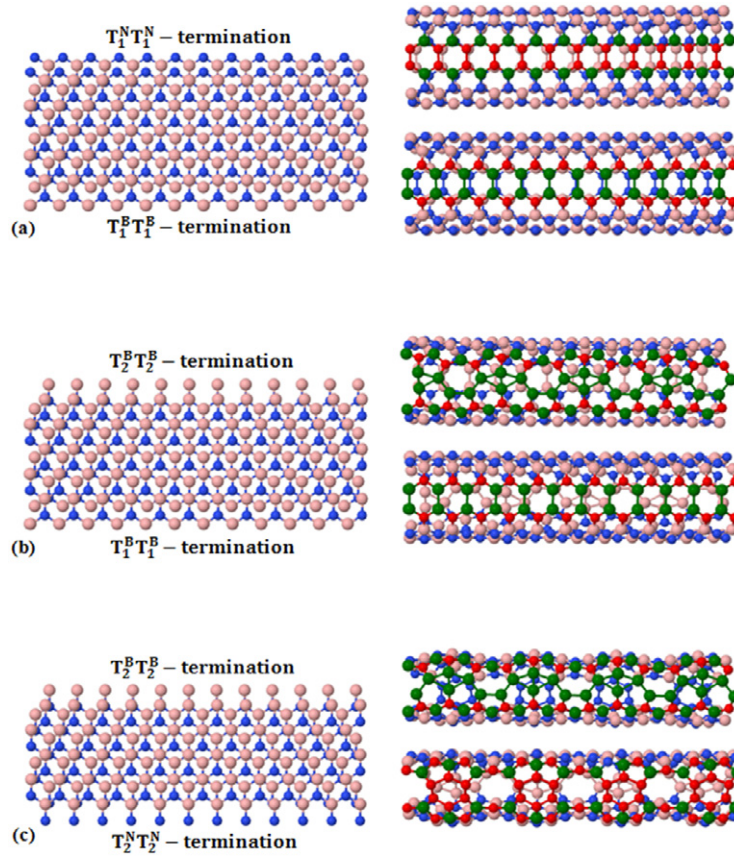


Figure 8. The top left sub-figures (a)–(c) show a supercell of AB-stacked of BiZBNRs (boron is shown in pink and nitrogen is shown in blue) with (a). $T_1^N T_1^N$ – termination. (top edge) and $T_1^B T_1^B$ – termination (bottom edge), comprising 240 nitrogen and boron atoms while the top right sub-figure shows the relaxed BN NT sculpture with two lines of hexagonal rings. In this case the top line contains a zip of hexagon rings, where each hexagonal ring contains four nitrogen atoms (red) and two boron atoms (green) while the bottom line contains a zip of hexagon rings, each hexagonal ring contains four boron atoms (green) and two nitrogen atoms (red). (b) $T_2^B T_2^B$ – termination (top edge) and $T_1^B T_1^B$ – termination (bottom edge), comprising 220 nitrogen and boron atoms while the top right sub-figure shows the relaxed BN NT sculpture with a top zip-line containing four-membered boron (three) rings, heptagons (four), horizontal pentagons pairs (three), pentagons (four) and horizontal hexagons pairs (three), the bottom zip-line contains hexagon rings with four boron atoms and two nitrogen atoms. (c) $T_2^B T_2^B$ – termination (top edge) and $T_2^N T_2^N$ – termination (bottom edge), comprising 200 nitrogen and boron atoms whilst the top right sub-figure shows the relaxed BN NT sculpture with a top zip-line containing four-membered boron rings (four), heptagons (three), horizontal pentagons pairs (four), pentagons (three) and horizontal hexagons pairs (four), the bottom zip-line contains hexagon rings of nitrogen (four), ten-membered boron and nitrogen ring (three) and horizontal pentagons pairs (eight). For clarity, in the defect lines all right sub-figures (a)–(c), boron is shown in green and nitrogen is shown in red.

unit cells (supercells). Using the DFT code SIESTA, results are obtained for the electronic density of states (DOS), the band structure and the number of open channels. Within a Landauer description of electron transport, since the CNTs investigated are periodic, the transmission

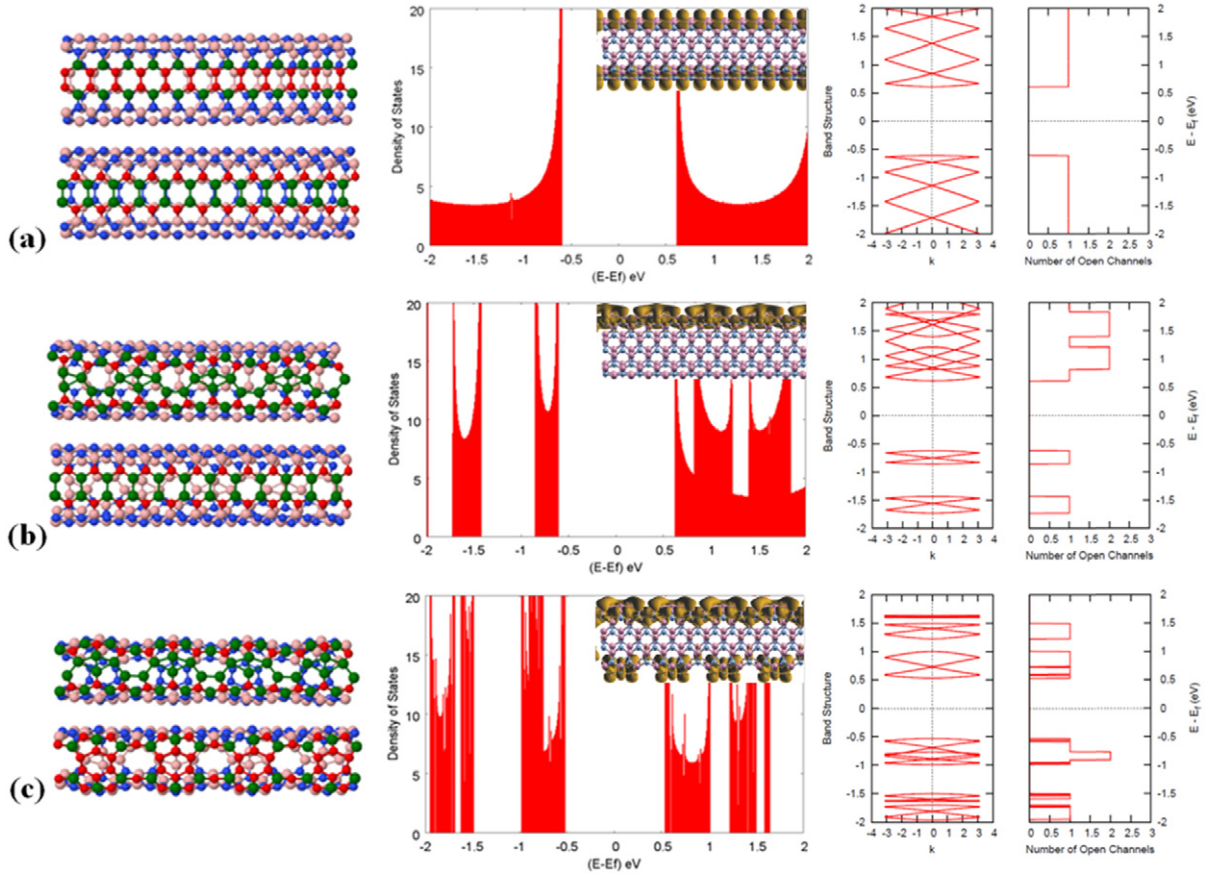


Figure 9. The left sub-figures (a)–(c) Show BNNT sculpturens (a) A BNNT sculpture with two zip-lines in the longitudinal direction comprising two lines of hexagonal rings. The top zip-line contains hexagon rings, where each ring contains four nitrogen atoms (red) and two boron atoms (green) whilst the bottom zip-line contains hexagon rings, each ring contains four boron atoms (green) and two nitrogen atoms (red). (b) A BNNT sculpture where the top zip-line contains four-membered boron (three) rings, heptagons (four), horizontal pentagons pairs (three), pentagons (four) and horizontal hexagons pairs (three) whilst the bottom zip-line contains hexagon rings with four boron atoms and two nitrogen atoms. (c) A BNNT sculpture with a top zip-line containing four-membered boron rings (four), heptagons (three), horizontal pentagons pairs (four), pentagons (three) and horizontal hexagons pairs (four) and the bottom zip-line containing hexagon rings of nitrogen (four), ten-membered boron and nitrogen ring (three) and horizontal pentagons pairs (eight). The middle and right sub-figures (a)–(c) show the DOS, band structures and number of open channels respectively. The calculations were carried out using 3000 k-points. The middle panes of each figure show the local densities of states of each sculpture (rotated by 90 degrees to aid visualization) in the vicinity of the Fermi energy.

coefficient $T(E)$ for electrons of energy E travelling from left to right is identical to the number of open channels and therefore the maximum current $I(V)$ carried by the CNTs at a finite voltage V , is given by:

$$I(V) = \frac{2e}{h} \int_{E_f - \frac{eV}{2}}^{E_f + \frac{eV}{2}} T(E) dE. \quad (1)$$

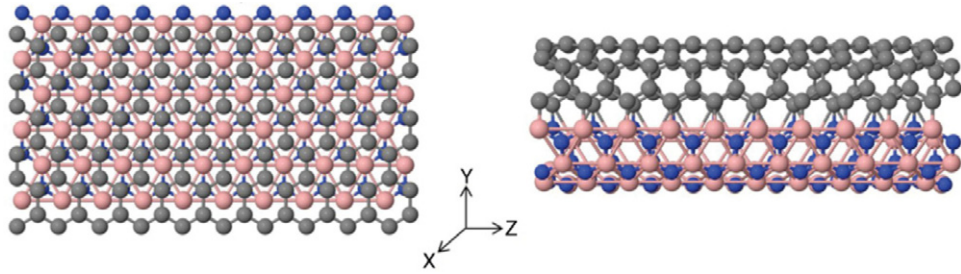


Figure 10. Left; a Super cell of *hetero*-bilayer NRs of boron nitride/graphene (periodic in z direction) which contains 240 atoms while the right sub-figure shows the relaxed (6,6) armchair hetero-NT obtained by relaxing the structure on the right.

As initial examples, figure 5 shows the DOS, band structure and number of open channels for the three CNT sculpturenes in figures 4(a), (c) and (g), which possess rather short unit cells in the horizontal direction. The sculpturenes shown in figures 5(a) and (c) are ideal NTs and possess the DOS of armchair and zigzag NTs respectively. In contrast, the CNT sculpturene shown in figure 5(b) contains a periodic line of 5/7 rings and the resulting DOS contains an energy gap near the Fermi energy of approximately 0.25 eV. This persistence of the energy gap is also found in CNTs containing periodic ‘zips’ of impurities [21, 22]. In all cases, the DOS contains van Hove singularities associated with the periodic nature of these quasi-one-dimensional structures.

The band structures and the number of open channels (equal to the number of mini-bands) at energy E for each system are shown in the far right of the figures. As expected, for the perfect (6,6) NT, we find a large interval of energy with two open channels near the Fermi energy, whereas the zigzag (8,0) NT possesses a gap at the Fermi energy[23]. The zipped NT with a periodic line of 5/7 rings possesses a smaller gap of 0.25 eV and exhibits a jump to either 1 or 2 open channels at the upper and lower band edges closest to the Fermi energy. As shown by the inset of figure 5(b), the states closest to the Fermi energy are concentrated on the zip of defects.

The DOS of examples of CNT sculpturenes with more complex unit cells are shown in figure 6. Figure 6(a) shows the CNT sculpturenes of figure 4(c), one side of which possesses a line of with nine pentagon/heptagon pairs and a diametrically-opposite side containing a line of eight pentagon/heptagon pairs per supercell. Figure 6(c) shows the CNT sculpturene of figure 4(e), one side of which possesses a line of nine vertical pentagon/heptagon pairs per supercell, while the opposite side contains four octagons, one horizontal pentagon-pair and three vertical pentagon-pairs per supercell. These show that in contrast with the energy gap shown in figure 5(b) there is almost no gap at Fermi energy and there is a corresponding increase in the electronic states around the Fermi energy.

For the sculpturene shown in figure 6(b), (which corresponds to the CNT sculpturene of figure 4(d)) the DOS shows many mini energy gaps around the Fermi energy. Similarly, figure 6(d) corresponds to a CNT sculpturene with one line of four octagons, one horizontal pentagon-pair and three vertical pentagon-pairs. The presence of quasi-disordered supercells in these sculpturenes leads to a significant increase in the DOS around the Fermi energy [24]. As shown by the insets of figure 5, the local-density-of-states close to the Fermi energy tends to be concentrated on these lines of defects.

From the number of open channels, it is clear that the conductance of sculpturenes with quasi-disordered unit cells is typically lower than that of conventional conducting NTs, because

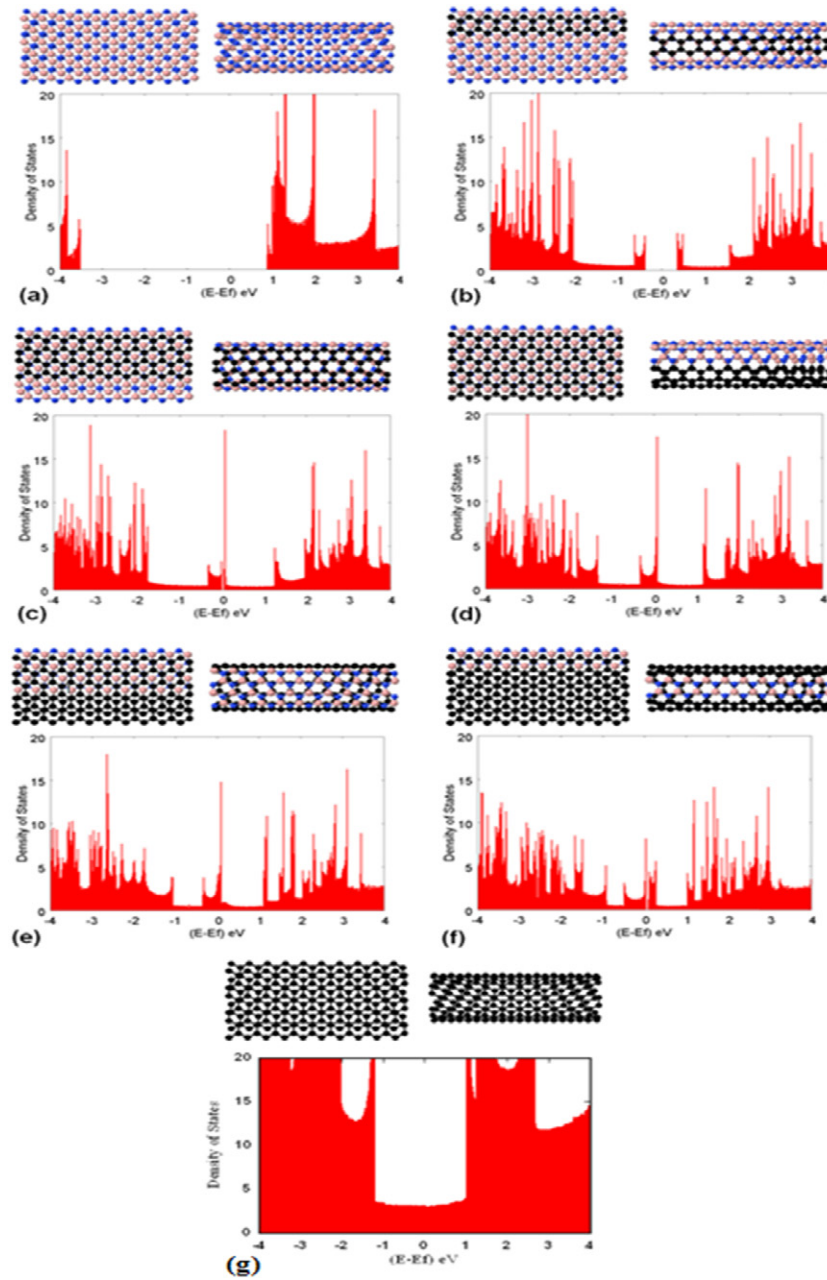


Figure 11. Panels (a) and (g) the top left sub-figures show AB-stacked bilayer BN and AB-stacked graphene NRs which are relaxed to form ideal BN and CNT sculpturenes (the top right sub-figures) respectively. (b) The top left sub-figures show AB-stacked hetero-bilayer NRs (the top layer with one-ring-thick graphene stacked on top of BNNR), the structure is relaxed to form a hetero-NT with one-ring-thick graphene (the top right sub-figure). (c) The top left sub-figures show AB-stacked hetero-bilayer NRs (the top layer with two-ring-thick graphene stacked on top of BNNR), the structure is relaxed to form a hetero-NT with two-ring-thick graphene (the top right sub-figure). (d) The top left sub-figures show AB-stacked hetero-bilayer NRs (the top layer is graphene NR stacked on top of BNNR), the structure is relaxed to form a hetero-NT consisting of a half a cylinder of carbon joined to a half cylinder of BN (the top right sub-figure).

Figure 11. (Continued) (e) The top left sub-figures show AB-stacked hetero-bilayer NRs (the top layer graphene NR is stacked on top of BNNR with one-ring-thick graphene), the structure is relaxed to form a hetero-NT with four-ring-thick graphene (the top right sub-figure). (f) The top left sub-figures show AB-stacked hetero-bilayer NRs (the top layer graphene NR stacked on top of BNNR with two-ring-thick graphene), the structure is relaxed to form a hetero-NT with five-ring-thick graphene (the top right sub-figure). All sub-figures on the bottom show the DOS of the hetero-NT sculpturenes calculated using 3000 k-points.

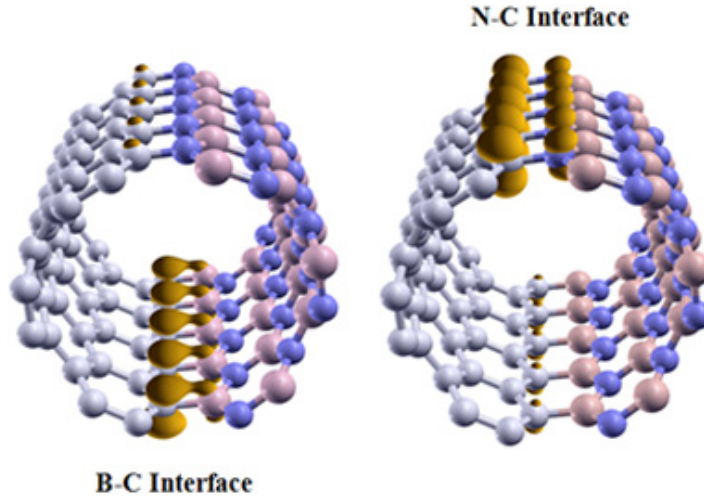


Figure 12. The left sub-figure shows that the LDOS (in yellow) of the sculpturene of figure 11(d) in the range $E = -0.35$ to -0.31 eV is concentrated at the boron–carbon interface (in yellow), while the LDOS in the range $E = 0.05$ to 0.09 eV shown in the right sub-figure is concentrated at the of nitrogen–carbon interface.

in the vicinity of the Fermi energy, the number of open channels rarely exceeds 2. Indeed evaluation of the current $I(V)$ defined by equation (1) confirms that the current is lower than that of a comparable ideal (6,6) NT.

3. Electronic properties of boron nitride (BN) sculpturenes formed from straight NRs

We now examine the electronic properties of BN sculpturenes. Conventional boron nitride nanotubes (BNNT) are quasi-one-dimensional nanostructures predicted in 1994 [25] and experimentally discovered in 1995. BN is an electrical insulator with a wide band-gap of approximately 5 eV [26–28]. In this section we examine the electronic properties of BNNT formed by relaxing bilayer BN NRs. As examples, figure 7 shows three different combinations of edge terminations of zigzag BN NRs.

When an AB-stacked bilayer is cut to form bilayer zigzag BN NRs, the bilayer NRs possess two upper and lower edges associated with each of the stacked monolayer ribbons. Each pair of upper (or lower) edges can be formed from a combination of the edges shown in figure 7. For bilayer zigzag BN NRs, examples of these combinations are shown in figures 8(a)–(c), along

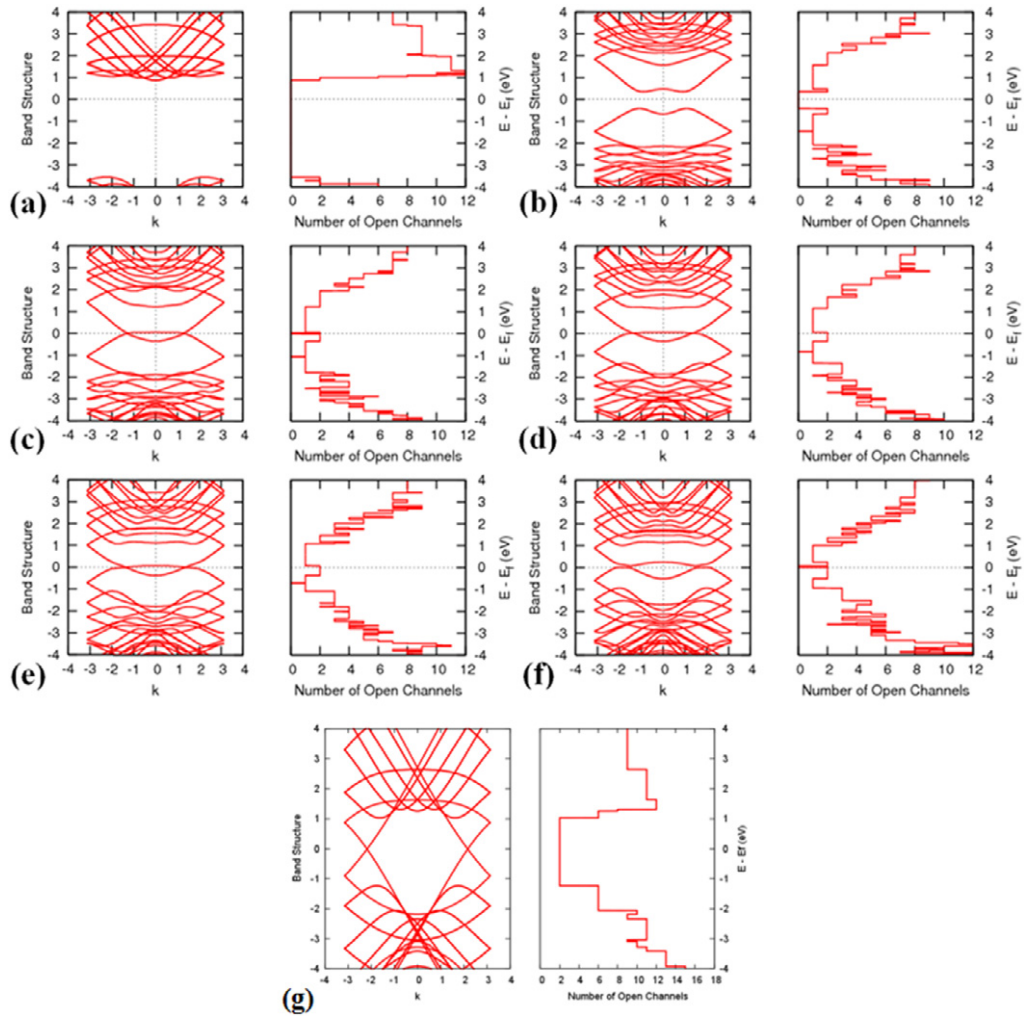


Figure 13. Panels (a)–(g) show the band structure and number of open channels for the hetero-NT sculpturenes shown in figures 11 (a)–(g) respectively. The calculations carried out with 3000 k -points.

with the resulting BN NTs following reconstruction. Each bilayer zigzag BN NR possesses a pair of upper-edge and lower-edge terminations, such as $T_1^N T_1^N$ and $T_1^B T_1^B$ in figure 8(a).

In contrast with the wide band gap of BN, the BN sculpturenes shown in figure 8 possess hugely-reduced gaps [29] of approximately 1.25 eV (figures 9(a)–(c)), which is similar to that of silicon (1.12 eV) [30]. Furthermore the BNNT sculpturenes in figures 9(b) and (c) possess additional energy gaps in the energy window from -2 to 2 eV.

The number of open channels for each system is shown in the far right sub-figures in figure 9. These show that within the energy window from -2 to 2 eV, there is only one open channel for the sculpturenes in figure 9(a) and one or two open channels for the others. Since the band gap is decreased in the zipped NTs, these can support current at low-bias voltages, which would not be possible in the insulating (6,6) BNNT.

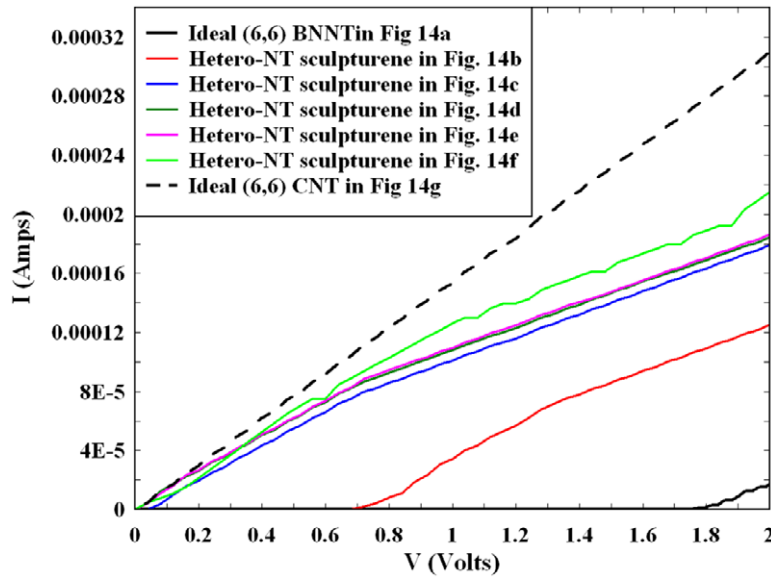


Figure 14. It shows I–V curve of the BNNT sculptures in figures 11(b)–(f).

4. Electronic properties of carbon-BN hetero-sculpturenes formed from straight NRs

In this section, we examine the electronic properties of hetero-NTs obtained by relaxing bilayer ribbons formed from a monolayer of carbon on top of a monolayer of BN. As an example, figure 10 shows the hetero-NT obtained by sculpting a hetero-bilayer from a monolayer of graphene on top of a single layer of BN and allowing reconstruction. The resulting NT consists of a half cylinder of carbon joined to a half cylinder of BN.

To understand the electronic structure of such hetero-sculpturenes, it is useful to examine their properties as a function of the relative widths of the carbon and BN sections of the NT. Such structures are likely to be challenging to realize experimentally, although in-plane junctions between monolayer BN and graphene are known [31] and therefore one can envisage cutting hetero-bilayer ribbons whose upper layer is formed in part from graphene and in part from BN, as shown in figure 11. This figure shows a range of resulting hetero-NTs, starting from (a) a perfect (6,6) BNNT, then containing progressively thicker sections of carbon (b–f) and ending with a perfect (6,6) CNT. In all cases, the hetero-NTs have a boron–carbon and a nitrogen–carbon interface and the overall structure is made of hexagonal rings.

These structures are useful for illustrating the role of the interface between graphene and BN, because they share features associated with impurities in CNTs [32–37], specifically those associated with the doping of CNTs with boron [27, 37] and nitrogen [24, 34]. For such impurities, a characteristic peak near the Fermi energy is found, with the peak associated with boron below the Fermi energy and the peak associated with nitrogen above the Fermi energy. Similar peaks appear in the DOS presented in figures 11(c)–(f). Beginning with the well-known DOS of the perfect (6,6) CNT (figure 11(g)), we see that the addition of a one-ring-thick NR of BN to the structure (figure 11(f)) creates a new feature near the Fermi energy. As the thickness of the BN strip increases (figures 11(e)–(c)), the feature persists. Since the feature has two peaks (one above and one below the Fermi energy), it is reasonable to expect the peaks are associated with either the boron–carbon interface or the nitrogen–carbon interface. To demonstrate this,

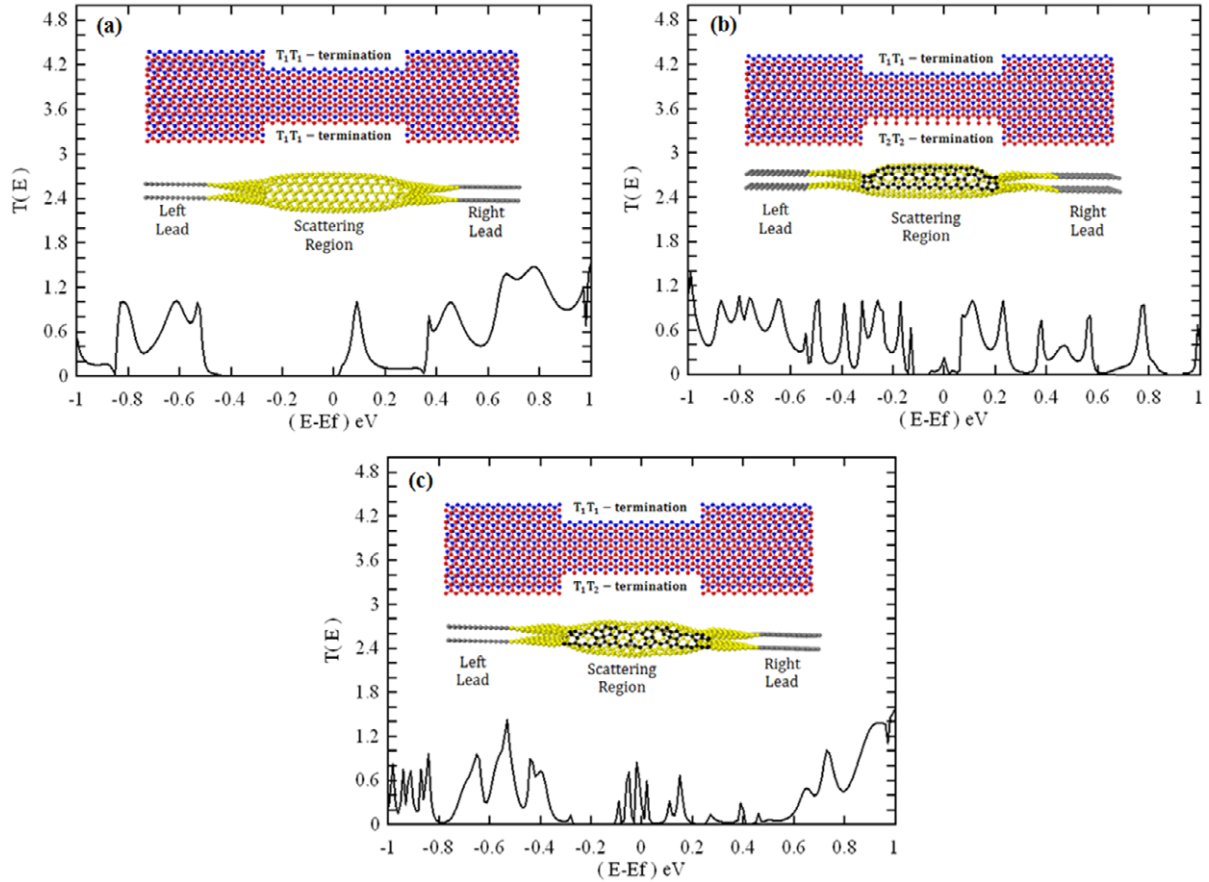


Figure 15. The inset figures show, (a) The initial supercell (top) which contains a sculpted NR region with T_1T_1/T_1T_1 -termination whose ends are connected to an AB-stacked BIG, the resulting sculpture is shown underneath the initial supercell (1224 carbon atoms). (b) The initial supercell (top) which contains a sculpted NR region with T_1T_1/T_2T_2 -termination whose ends are connected to an AB-stacked BIG, the resulting sculpture is shown underneath the initial supercell (1198 carbon atoms). (c) The initial supercell (top) which contains a sculpted NR region with T_1T_1/T_1T_2 -termination whose ends connected to AB-stacked BIG, the resulting sculpture is shown underneath the initial supercell (1211 carbon atoms). The black curves represent the zero bias transmission probability of the CNT sculptures which are connected to BiG electrodes after relaxation. See movies 2 and 3, available at stacks.iop.org/NJP/16/013060/mmedia.

figure 12 shows the local density of states (LDOS) for the structure of figure 11(d), centred on each peak. The orbital distributions shown in figure 12 were obtained by calculating the LDOS in a 0.04 eV of energy window centred on the two peaks shown in figure 11(d). Clearly, the peaks are localized at the two interfaces. Figure 11(b) shows that adding a one-ring-thick graphene NR to a BN NT significantly reduces the gap to approximately 0.8 eV, while the addition of a two-ring-thick graphene NR closes the gap completely. Interestingly, the two-peak feature associated with the boron–carbon and nitrogen–carbon interfaces is robust, being present even in figure 11(b).

The band structures and number of open channels for these hetero-NTs are shown in figure 13. With the obvious exceptions of the perfect BNNT and CNT and the one-ring-thick

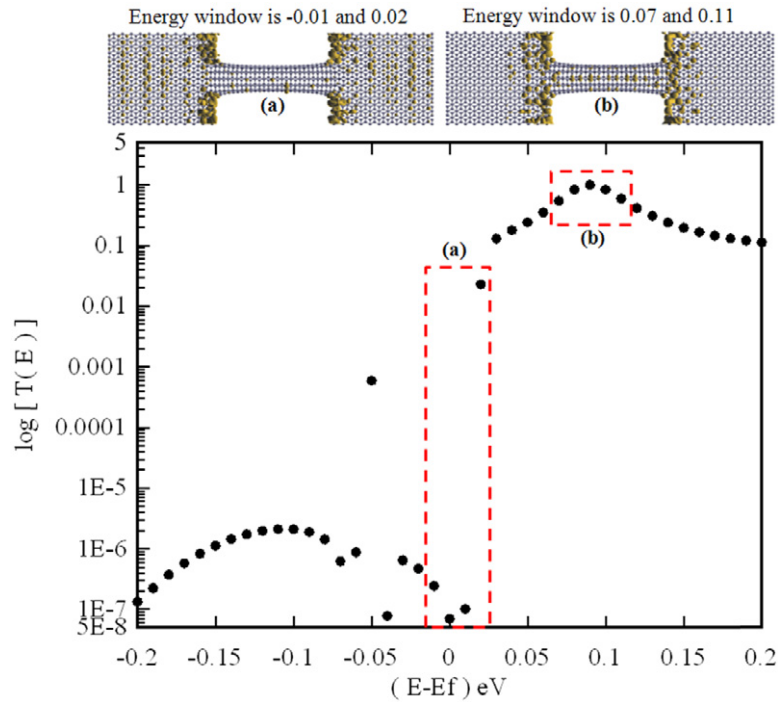


Figure 16. Panels (a) and (b) show the LDOS of the sculpturene shown in figure 15(a). The bottom figure shows the transmission probability in logarithm scale; the red dotted rectangles highlighted the energy ranges which are corresponding to the energy ranges of the LDOS.

graphene NR structure which possesses a band gap, the electronic structures are remarkably similar. As a consequence the I–V curves in figure 14 (obtained from equation (1)) are also similar for all of these hetero-NTs, with the exception of the sculpturenes of figure 11(b).

5. Electronic properties of sculpturenes with sculpted electrodes

One of the biggest challenges for future nanoelectronics is the design of reliable methods to connect sub-10 nm devices to electrodes. As illustrated in figures 15 and 20, sculpturenes have the potential to overcome this contacting problem. As an example, figure 15 shows that by sculpting a narrow rectangular BiGNR between two wider BiGNRs and allowing them to relax, the resulting sculpturene is a CNT automatically connected to BiGR electrodes. As a second example, figure 20 shows that more complex structures, such as a CNT torus connected to electrodes can also be obtained. The structures of figures 15 and 20 comprise a central scattering region attached to periodic electrodes on the left and right and therefore their transmission coefficients $T(E)$ can be obtained using the non-equilibrium Green's function code SMEAGOL [38, 39], which utilizes the DFT-based hamiltonian from SIESTA. In what follows, we investigate the transport properties of such sculpturene-based systems, which are constructed by sculpting a finite AB-stacked BiGNR (with the same terminations shown in figures 4(a)–(f) whose ends are connected to periodic BiGR electrodes.

Figure 15(a) shows the transmission probability of sculpturene obtained by sculpting a NR from AB-stacked BiG with T_1T_1/T_1T_1 termination, while figures 15(b) and (c) show the

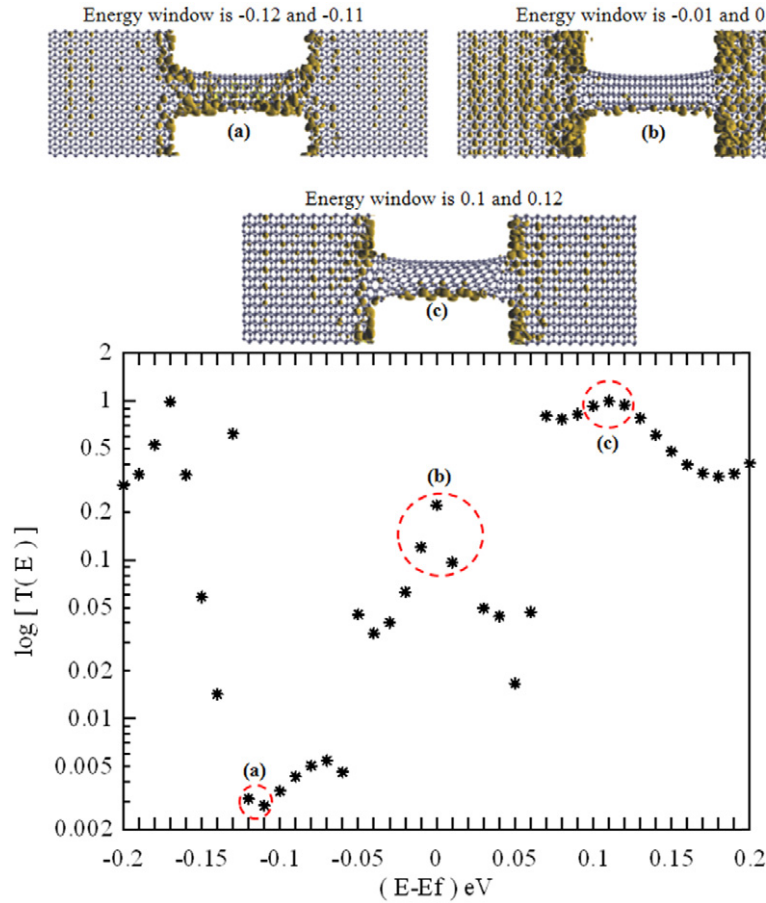


Figure 17. Panels (a)–(c) show the LDOS of the sculpturene shown in figure 15(b). The bottom figure shows the transmission probability in logarithm scale; the red dotted circles highlighted the energy ranges which correspond to the energy ranges of the LDOS.

transmission probability of zipped sculpturenes obtain by sculpting NRs from AB-stacked BiGR with T_1T_1/T_2T_2 and T_1T_1/T_1T_2 terminations respectively and then relaxing the initial structures to form CNT sculpturenes which are automatically connected to AB-stacked BiG electrodes.

Figure 15(a) shows that compared with the $T(E)$ of the (6,6) CNT obtained from the T_1T_1/T_1T_1 terminations shown in figure 5(a), there is a significant reduction in $T(E)$ at the Fermi energy, whereas there is an enhancement in the $T(E)$ at Fermi energy of the sculpturenes in figures 15(b) and (c), which contain lines of non-hexagonal rings and correspond to the T_1T_1/T_2T_2 and T_1T_1/T_1T_2 terminations of figures 6(a) and (d).

To illustrate the origin of these features in $T(E)$, the local densities of states (LDOS) of the sculpturenes in figures 15(a) and (b) are shown in figures 16 and 17 respectively, within narrow energy ranges of interest near the Fermi energy.

Figure 16 shows that the low value of $T(E)$ near the Fermi energy for the sculpturene of figure 15(a) is associated with the absence of states in the central CNT region at this energy, whereas the higher transmission in energy region *b* arises from the presence of an extended state within the central CNT. In contrast, figure 17 shows that the LDOS at and around Fermi

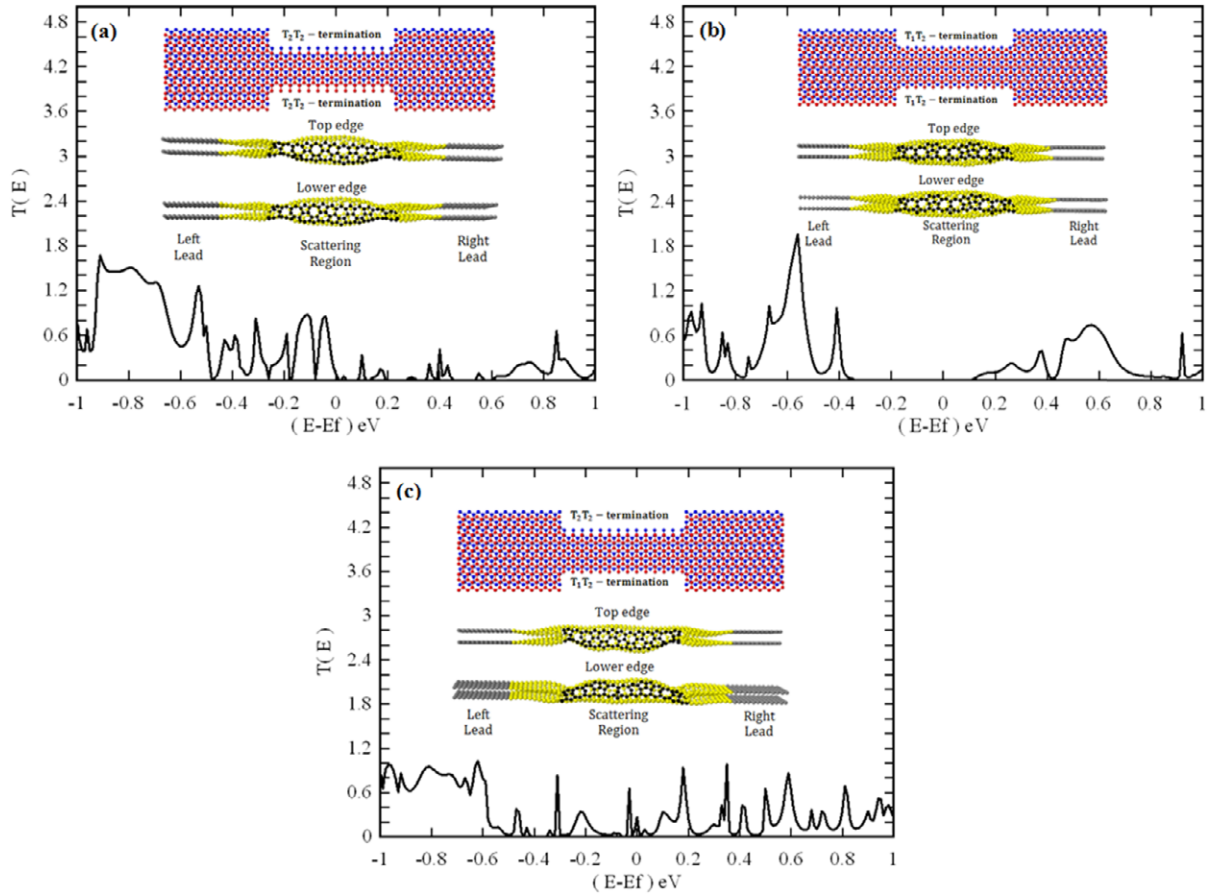


Figure 18. The inset figures show, (a) The initial supercell (top) which contains a sculpted NR region with T_2T_2/T_2T_2 -termination whose ends connected to AB-stacked BIG, the resulting sculpture is shown underneath the initial supercell (1172 carbon atoms). (b) The initial supercell (top) which contains a sculpted NR region with T_1T_2/T_1T_2 -termination whose ends connected to AB-stacked BIG, the resulting sculpture is shown underneath the initial supercell (1198 carbon atoms). (c) The initial supercell (top) which contains a sculpted NR region with T_2T_2/T_1T_2 -termination whose ends connected to AB-stacked BIG, the resulting sculpture is shown underneath the initial supercell (1185 carbon atoms). The black curves represent the zero bias transmission probability of the CNT sculptures which are connected to BiG electrodes after relaxation.

energy of the CNT sculpture of figure 15(b) is non-zero along the lines of 5/7 rings, which leads to the relatively-high conductance of this sculpture system.

Figures 18(a), 5, 13(b) and 18(c) show the transmission probability of quasi-disordered sculptures (with two lines of non-hexagon rings) which are obtained by sculpting a NR from AB-stacked BiG with T_2T_2/T_2T_2 , T_1T_2/T_1T_2 and T_2T_2/T_1T_2 terminations respectively and allow them to reconstruct.

Like the structures of figures 15(b) and 17, the non-hexagonal carbon rings which appear in the final sculptures again strongly influence transport. The left sub-figure of figure 19 shows that at low voltages, the sculptures shown in figures 15(a) and (c) can carry the higher currents, while at higher voltages between approximately 0.2 and 1.4 V, the structure shown

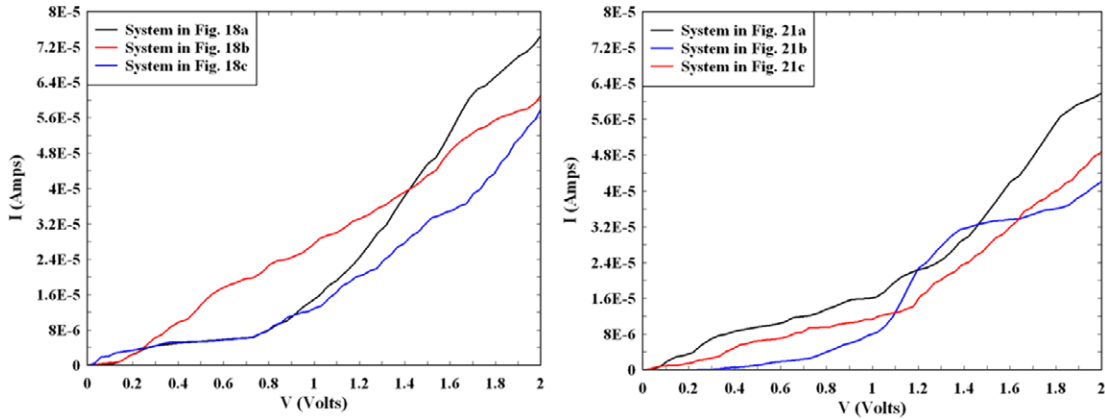


Figure 19. Shows I–V curve of the sculpture systems shown in figures 15 and 18. The left sub-figure shows the I–V curve of the systems in figures 15(a)–(c). The right sub-figure shows the I–V curve of the systems in figures 18(a)–(c).

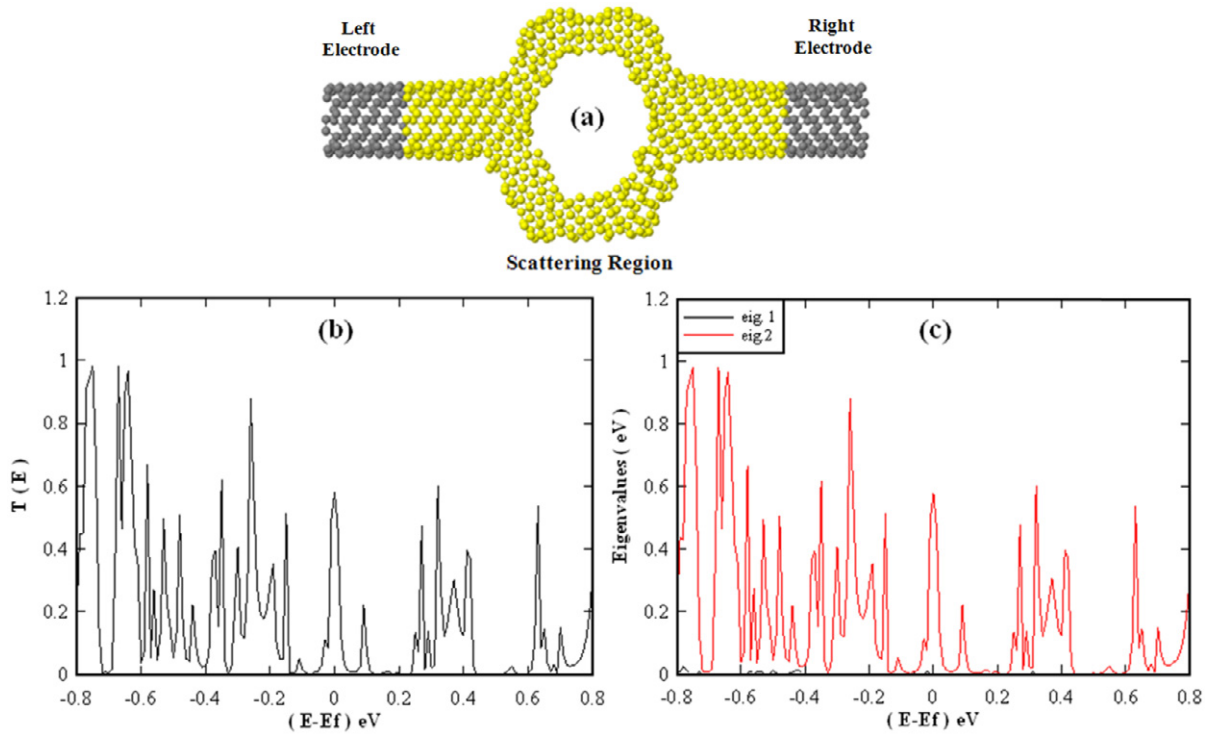


Figure 20. (a) Shows a torus sculpture system. (b) Shows the zero bias transmission probability. (c) Shows the two eigenvalues which correspond to the two open channels in the right lead, the red curve represents the dominant eigenvalue and the black curve is the non-dominant eigenvalue. See movie 4, available at stacks.iop.org/NJP/16/013060/mmedia.

in figure 15(b) carries the higher current. Similarly the right sub-figure shows the sculpture system with two lines of 5/7 rings (figure 18(a)) carries the higher current up to approximately 1 V, whereas the lower current corresponds to the system shown in figure 18(b).

Over a range of energies near the Fermi energy, the value of $T(E)$ shown in figures 15 and 18 never exceeds unity. To illustrate that this feature is shared by other in-situ sculptures,

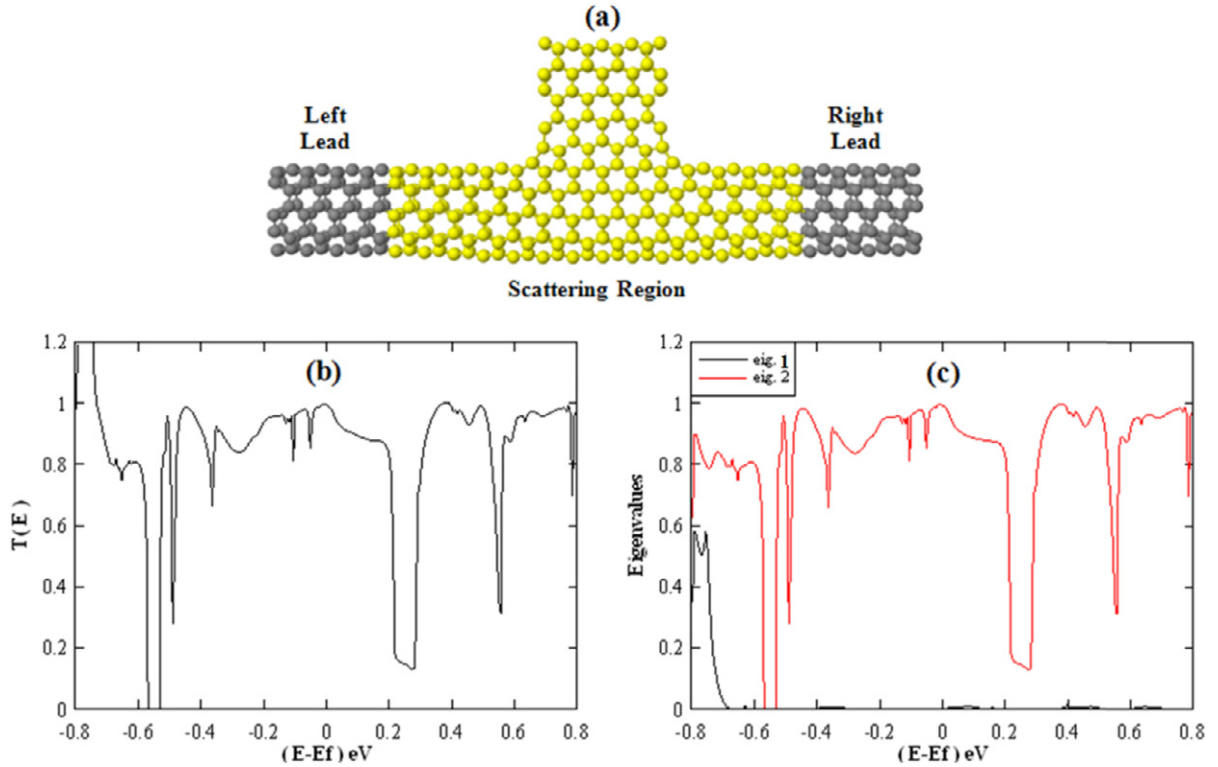


Figure 21. (a) Shows the nanobud sculpture. (b) Shows the zero bias transmission probability of the nanobud sculpture. (c) Shows the two eigenvalues which are corresponding to the two open channels in the leads, the black curve shows the non-dominant eigenvalue and the red curve shows the dominant eigenvalue.

we now compute $T(E)$ for the torus of figure 20(a) and the carbon nanobud-like structure of figure 21(a).

For the structure in figure 20(a), there are two open scattering channels in the energy range of from -0.8 to 0.8 eV and therefore in this range, the transmission matrix \vec{t} is a 2×2 matrix of the form:

$$\vec{t} = \begin{pmatrix} t_{11} & t_{12} \\ t_{21} & t_{22} \end{pmatrix}. \quad (2)$$

The transmission coefficient $T(E)$ is therefore equal to the sum of the two eigenvalues of the transport matrix τ , given by:

$$\tau = \vec{t}\vec{t}^\dagger \quad (3)$$

Figure 20(b) shows a plot of $T(E)$, while figure 20(c) shows plots of the two eigenvalues. One of the two eigenvalues is dominant (red curve) whereas the second eigenvalue (black curve) is negligible.

The presence of a single dominant transmission eigenvalue is also found in of the carbon nanobud-like structure shown in figure 21(a), whose $T(E)$ is shown in figure 21(b). Figure 21(c) again shows that this sculpture possesses single dominant eigenvalue (red curve) and a negligible second eigenvalue (black curve).

The presence of a single dominant channel, with $T(E)$ never exceeding unity is typical of electron transport through single molecules, where the $T(E)$ exhibit Breit–Wigner and/or

Fano resonances when E coincides with molecular energy levels (shifted by the self-energy of the electrodes) [40]. Hence the sculpturenes of figures 15–21 share the advantages of single-molecule devices associated with the presence of transport resonances, but do not suffer from the well-known disadvantages associated with highly-resistive contacts to the electrodes. Like single-molecule devices [41], transport through the above structures is also controlled by geometry, but on a significantly-higher length scale.

6. Summary

The electronic properties of carbon, BN and BN–carbon-based sculpturenes have been investigated.

For the simplest sculpturenes formed from reconstructed BiGNRs, the resulting NTs depend not only on the chirality of the initial NRs, but also on the combination of edge terminations. Typically the sculpturene NTs possess a unit cell which is longer than the initial BiGNR and in many cases possess lines of non-hexagonal rings, which as shown in figure 6, lead to a reduction or even elimination of energy gaps in the DOS of such structures. For BN sculpturenes, figure 9 shows that the energy gap near the Fermi energy is found to persist, but is significantly reduced for the bulk value. In the case of hetero-NT sculpturenes formed from reconstructed ribbon containing both carbon and BN strips, pronounced peaks in the DOS are found, which arise from carbon–boron and carbon–nitrogen bonds. Sculpturenes connected to sculpted electrodes have also been investigated, including NT-like structures, a torus and a nanobud. In all cases, electron transport was found to be dominated by a single scattering channel, leading to electrical conductance less than or of order the conductance quantum.

The above examples demonstrate that electronic properties such as the band gap and electrical conductance of sculpturenes can be tuned by varying the geometry of the initially-sculpted bilayers, or in the case of hetero-structures, by varying the relative concentrations of the two materials. Furthermore their connectivity to external electrodes can be engineered in a controlled manner, thereby offering a new approach to optimizing contact resistances. In addition to the sculpturenes considered here, one can envisage many other examples, including sculpturenes formed from other 2d materials and combinations thereof. In addition, under realistic conditions, the initially-cut bilayer structures may have disordered edges, which would add to the variety of achievable sculpturenes. On the other hand, a molecular dynamics study of defective CNTs at 1500 K has shown an interesting self-healing property [42], which suggests that, at moderate temperature, the disorder in these NTs may ‘heal’ into a smaller set of stable structures of the type considered in this paper. For the future it would be of interest to the self-healing properties of sculpturenes and their atomic-scale dynamics during simultaneous cutting and reconstruction.

References

- [1] Qi J S, Huang J Y, Feng J, Shi D N and Li J 2011 The possibility of chemically inert, graphene-based all-carbon electronic devices with 0.8 eV gap *ACS Nano* **5** 3475–82
- [2] Algharagholy L, Bailey S W D, Pope T and Lambert C J 2012 Sculpting molecular structures from bilayer graphene and other materials *Phys. Rev. B* **86** 075427
- [3] Feng J, Li W, Qian X, Qi J, Qi L and Li J 2012 Patterning of graphene *Nanoscale* **4** 4883–99

- [4] Han M Y, Özyilmaz B, Zhang Y and Kim P 2007 Energy band-gap engineering of graphene nanoribbons *Phys. Rev. Lett.* **98** 206805
- [5] Chen Z, Lin Y-M, Rooks M J and Avouris P 2007 Graphene nano-ribbon electronics *Phys. E: Low-Dimens. Syst. Nanostruct.* **40** 228–32
- [6] Tapasztó L, Dobrik G, Lambin P and Biró L P 2008 Tailoring the atomic structure of graphene nanoribbons by scanning tunnelling microscope lithography *Nature Nanotechnol.* **3** 397–401
- [7] Datta S S, Strachan D R, Khamis S M and Johnson C A T 2008 Crystallographic etching of few-layer graphene *Nano Lett.* **8** 1912–5
- [8] Ci L, Xu Z, Wang L, Gao W, Ding F, Kelly K F, Yakobson B I and Ajayan P M 2008 Controlled nanocutting of graphene *Nano Res.* **1** 116–22
- [9] Campos L C, Manfrinato V R, Sanchez-Yamagishi J D, Kong J and Jarillo-Herrero P 2009 Anisotropic etching and nanoribbon formation in single-layer graphene *Nano Lett.* **9** 2600–4
- [10] Campos-Delgado J *et al* 2008 Bulk production of a new form of sp² carbon: crystalline graphene nanoribbons *Nano Lett.* **8** 2773–8
- [11] Li X, Wang X, Zhang L, Lee S and Dai H 2008 Chemically derived, ultrasmooth graphene nanoribbon semiconductors *Science* **319** 1229–32
- [12] Wu Z-S, Ren W, Gao L, Liu B, Zhao J and Cheng H M 2010 Efficient synthesis of graphene nanoribbons sonochemically cut from graphene sheets *Nano Res.* **3** 16–22
- [13] Lee J *et al* 2013 Direct visualization of reversible dynamics in a Si₆ cluster embedded in a graphene pore *Nature Commun.* **4** 1650
- [14] Robertson A W *et al* 2012 Spatial control of defect creation in graphene at the nanoscale *Nature Commun.* **3** 1144
- [15] Soler J M *et al* 2002 The SIESTA method for *ab initio* order-*N* materials simulation *J. Phys.: Condens. Matter* **14** 2745
- [16] Lambert C J and Weaire D 1981 Theory of the arrangement of cells in a network *Metallography* **14** 307–18
- [17] Lambert C J and Weaire D 1983 Order and disorder in 2D random networks *Phil. Mag. B* **47** 445–50
- [18] Chen L, Ouyang Y, Wang Y, Sun Y and Pan H 2010 The influence of Stone–Wales defects on magnetic properties in graphene *Phys. E: Low-Dimens. Syst. Nanostruct.* **43** 593–7
- [19] Yu D, Lupton E M, Liu M, Liu W and Liu F 2008 Collective magnetic behavior of graphene nanohole superlattices *Nano Res.* **1** 56–62
- [20] Duplock E J, Scheffler M and Lindan P J 2004 Hallmark of perfect graphene *Phys. Rev. Lett.* **92** 225502
- [21] Sternberg M *et al* 2006 Carbon Ad-dimer defects in carbon nanotubes *Phys. Rev. Lett.* **96** 075506
- [22] Chico L 1996 Quantum conductance of carbon nanotubes with defects *Phys. Rev. B* **54** 2600–6
- [23] Saito R, Dresselhaus G and Dresselhaus M S 1998 *Physical Properties of Carbon Nanotubes* vol 35 (Singapore: World Scientific)
- [24] Charlier J-C 2002 Defects in carbon nanotubes *Acc. Chem. Res.* **35** 1063–9
- [25] Rubio A, Corkill J L and Cohen M L 1994 Theory of graphitic boron nitride nanotubes *Phys. Rev. B* **49** 5081
- [26] Golberg D and Sekiguchi T 2005 Perfectly dissolved boron nitride nanotubes due to polymer wrapping *J. Am. Chem. Soc.* **127** 15996–97
- [27] Goldberg D *et al* 2010 Boron nitride nanotubes and nanosheets *ACS Nano* **4** 2979–93
- [28] Chopra N G *et al* 1995 Boron nitride nanotubes *Science* **269** 966–7
- [29] Li X, Wu X, Zeng X C and Yang J 2012 Band-gap engineering via tailored line defects in boron-nitride nanoribbons, sheets, and nanotubes *ACS Nano* **6** 4104–12
- [30] Luppi M and Ossicini S 2005 *Ab initio* study on oxidized silicon clusters and silicon nanocrystals embedded in SiO₂: beyond the quantum confinement effect *Phys. Rev. B* **71** 035340
- [31] Liu Z *et al* 2013 In-plane heterostructures of graphene and hexagonal boron nitride with controlled domain sizes *Nature Nanotechnol.* **8** 119–24
- [32] Peng S and Cho K 2003 *Ab initio* study of doped carbon nanotube sensors *Nano Lett.* **3** 513–17
- [33] Reyes S A, Struck A and Eggert S 2009 Lattice defects and boundaries in conducting carbon nanotubes *Phys. Rev. B* **80** 075115

- [34] Wiggins-Camacho J D and Stevenson K J 2009 Effect of nitrogen concentration on capacitance, density of states, electronic conductivity, and morphology of *N*-doped carbon nanotube electrodes *J. Phys. Chem. C* **113** 19082–90
- [35] Moradian R 2004 Disordered carbon nanotube alloys in the effective-medium supercell approximation *Phys. Rev. B* **70** 205425
- [36] Liu Y and Guo H 2004 Current distribution in *B*- and *N*-doped carbon nanotubes *Phys. Rev. B* **69** 115401
- [37] Carroll D L *et al* 1998 Effects of nanodomain formation on the electronic structure of doped carbon nanotubes *Phys. Rev. Lett.* **81** 2332–5
- [38] Rocha A R *et al* 2006 Spin and molecular electronics in atomically generated orbital landscapes *Phys. Rev. B* **73** 085414
- [39] Rocha A R *et al* 2005 Towards molecular spintronics *Nature Mater.* **4** 335–9
- [40] Papadopoulos T, Grace I and Lambert C J 2006 Control of electron transport through Fano resonances in molecular wires *Phys. Rev. B* **74** 193306
- [41] Finch C M, Sirichantaropass S, Bailey S, Grace I, García-Suarez V and Lambert C J 2008 Conformation dependence of molecular conductance: chemistry versus geometry *J. Phys.: Condens. Matter* **20** 022203
- [42] Zhang C-L and Shen H-S 2007 Self-healing in defective carbon nanotubes: a molecular dynamics study *J. Phys.: Condens. Matter* **19** 386212